

Article

# Electrophoretic Deposition and Characteristics of Chitosan–Nanosilver Composite Coatings on a Nanotubular TiO<sub>2</sub> Layer

Michał Bartmański <sup>1,\*</sup>, Łukasz Pawłowski <sup>1</sup>, Andrzej Zieliński <sup>1</sup>, Aleksandra Mielewczyk-Gryń <sup>2</sup>, Gabriel Strugała <sup>1</sup> and Bartłomiej Cieślik <sup>3</sup>

<sup>1</sup> Department of Materials Engineering and Bonding, Gdańsk University of Technology, Narutowicza 11/12, 80-233 Gdansk, Poland; lukasz.pawlowski@pg.edu.pl (Ł.P.); andrzej.zielinski@pg.edu.pl (A.Z.); gabriel.strugala@pg.edu.pl (G.S.)

<sup>2</sup> Department of Solid State Physics, Gdańsk University of Technology, Narutowicza 11/12, 80-233 Gdansk, Poland; alegryn@pg.edu.pl

<sup>3</sup> Department of Analytical Chemistry, Gdańsk University of Technology, Narutowicza 11/12, 80-233 Gdansk, Poland; bartlomiej.cieslik@pg.edu.pl

\* Correspondence: michal.bartmanski@pg.edu.pl; Tel.: +48-500-034-220

Received: 28 January 2020; Accepted: 3 March 2020; Published: 6 March 2020



**Abstract:** The surface treatment of titanium implants has been applied mainly to increase surface bioactivity and, more recently, to introduce antibacterial properties. To this end, composite coatings have been investigated, particularly those based on hydroxyapatite. The present research was aimed at the development of another coating type, chitosan–nanosilver, deposited on a Ti13Zr13Nb alloy. The research comprised characterization of the coating’s microstructure and morphology, time-dependent nanosilver dissolution in simulated body fluid, and investigation of the nanomechanical properties of surface coatings composed of chitosan and nanosilver, with or without a surface-active substance, deposited at different voltages for 1 min on a nanotubular TiO<sub>2</sub> layer. The microstructure, morphology, topography, and phase composition were examined, and the silver dissolution rate in simulated body fluid, nanoscale mechanical properties, and water contact angle were measured. The voltage value significantly influenced surface roughness. All specimens possessed high biocompatibility. The highest and best adhesion of the coatings was observed in the absence of a surface-active substance. Silver dissolution caused the appearance of silver ions in solution at levels effective against bacteria and below the upper safe limit value.

**Keywords:** bioactive coatings; chitosan coatings; antibacterial coatings; silver release; nanomechanical properties; wettability

## 1. Introduction

Titanium and its alloys are the most promising biomaterials applied for long-term orthopedic, dental, and maxillofacial implants. Among the many titanium alloys, the Ti13Zr13Nb alloy seems to be the best choice compared to the widely used commercial Ti-6Al-4V and Ti-6Al-7Nb alloys, as it possesses Young’s modulus approaching that of a bone, and it contains no harmful elements such as Al or V [1].

The rejection of long-term implants observed during the primary and long-term fixation period has resulted in the development of a variety of antibacterial titanium surfaces for titanium implants, with the most popular including Ag, Cu, Zn, F, Y, Fe, N, Co, antibiotics, chitosan, and peptides [2,3]. Silver is used in medical applications as pure metallic silver, silver halides, nitrate, and sulfate, silver–organic complexes and silver zeolite, silver oxide nanoparticles, and silver ions [4–6]. Silver nanoparticles

(AgNPs) cause damage to the bacterial membrane and subcellular structures, dependent on the shape, size, surface appearance, and chemical states, and aggregation of the AgNPs [7].

Chitosan is a chemical compound with specific antibacterial properties [2,8–10]. Its main medical applications include controlled drug delivery, wound healing, and tissue regeneration [11,12]. Multiple coatings have been developed to improve these biological properties. Chitosan–AgNP coatings showed an inhibitory effect on the growth of some pathogens and reduced biofilm formation with no observed cell cytotoxicity in one study [13]. In another study, chitosan-based films containing silver nanoparticles were shown to have wetting properties highly sensitive to the fraction of AgNPs [14]. Coatings composed of chitosan, silver, and hydroxyapatite exhibited antibacterial activity and were nontoxic to MC3T3-E1 cells [15]; chitosan coatings with silver-decorated calcium phosphate microspheres lowered bacterial viability up to 90% [16], and silver-doped  $\beta$ -tricalcium phosphate composite coatings exhibited antibacterial activity and no adverse cytotoxic effects towards the cell line MG-63 [17]. Chitosan–cellulose composite films with AgNPs demonstrated excellent antibacterial properties against *Escherichia coli* and *Staphylococcus aureus* [18]. Coatings comprising polyvinyl alcohol capped with silver nanoparticles and based on a chitosan matrix demonstrated bactericidal activity against *E. coli* and *S. aureus* [19]. Finally, chitosan–gelatin–nanosilver composite films also showed in vitro antibacterial activity against *E. coli* and *S. aureus* [20].

Similar antibacterial effectiveness was also exhibited by nanocomposites of chitosan and nanosilver, which demonstrated significant antimicrobial activity against Gram-negative *Salmonella* and a potent anticancer effect [21], reduced fungal growth and caused morphological and ultrastructural changes in the pathogen [22], and were effective against *S. aureus*, *Bacillus sp.*, *E. coli*, *Proteus sp.*, *Pseudomonas sp.*, *Serratia sp.*, and *Klebsiella sp.* and the fungal pathogens *Aspergillus niger*, *Aspergillus flavus*, *Aspergillus fumigatus*, and *Candida albicans* [23]. Such nanocomposites demonstrated minimum bactericidal concentration values of 39.1 and 312.5  $\mu\text{g/ml}$  for *E. coli* and *S. aureus*, respectively, and did not exhibit cytotoxicity to L-929 fibroblasts [24]. Chitosan hydrogels, reinforced with silver nanoparticles, revealed ultra-high mechanical and high antibacterial properties against *E. coli* and *S. aureus* and were used to accelerate wound healing [25].

The fundamental problem in the deposition of chitosan coatings is the perfect dispersion of nanosilver particles in such coatings. To introduce and maintain dispersion in an electrolyte, numerous surface dispersing agents are added to the bath, such as Tween 20, Tween 80, sodium dodecyl sulfate, trisodium citrate, and Span 20 [26–30]. Among these, polysorbate 20 (Tween 20) is often used for chitosan coatings because it provides a more stable, less aggregated suspension of metallic nanoparticles. Furthermore, it reduces the interfacial tension and improves the adhesion of the chitosan coating to the substrate [31,32].

All research conducted to date has clearly shown that chitosan–AgNP coatings demonstrate high antibacterial efficacy against a significant number of Gram-positive and Gram-negative strains, including fecal bacteria. However, the mechanical properties of such material systems, determined for thin layers mainly via phenomena occurring at titanium–chitosan/AgNPs interfaces, and the surface state have been much less investigated. In the present research, a nanotubular oxide layer was created and used to improve the adhesion of chitosan–AgNP coatings obtained by electrophoretic deposition (EPD), a technical solution often applied for different coatings, but seldom for the one investigated here. Adhesion was also determined by the chemistry of the metallic surface, and the presented research is likely the first study of this nature to apply the Ti13Zr13Nb alloy, the safest of all the titanium materials applied for load-bearing implants.

## 2. Materials and Methods

### 2.1. Preparation of Specimens

The Ti13Zr13Nb alloy (SeaBird Metal Materials Co., Baoji, China) used as a substrate had the composition shown in Table 1. Round samples, 4 mm thick, and with a 3.14  $\text{cm}^2$  area, were cut from rods of 40 mm diameter. The surface roughness was  $S_a = 0.15 \mu\text{m}$ , achieved by polishing with abrasive

sandpapers, with No. 2000 as the last. Subsequently, the specimens were rinsed in pure isopropanol and then in deionized water with an ultrasonic device (Sonic-3, POLSONIC, Warsaw, Poland) for 15 min. Finally, etching was performed for 10 min in 25% HNO<sub>3</sub> to remove the native oxide layers [33], after which the samples were once again rinsed with distilled water and air-dried.

**Table 1.** The chemical composition of the Ti13Zr13Nb alloy, wt.%.

Element	Nb	Zr	Fe	C	N	O	Ti
wt.%	13.0	13.0	0.05	0.04	0.019	0.11	remainder

### 2.2. Electrochemical Oxidation of Ti13Zr13Nb Alloy

Electrochemical oxidation was done in a test solution of 10 mL of 85% orthophosphoric acid (1M H<sub>3</sub>PO<sub>4</sub>) (Sigma Aldrich), 1.2 mL of 40% of hydrofluoric acid (HF) (both from Polskie Odczynniki Chemiczne, Gliwice, Poland), and 150 mL of deionized water. The tests were carried out in a standard electrical circuit comprising an electrochemical cell, a DC power source (MCP/SPN110-01C, Shanghai MCP Corp., Shanghai, China), a platinum polarising electrode as the cathode, and the tested alloy as the anode, placed at a distance of 10 mm. All tests were carried out at room temperature, at a constant voltage of 20 V, and a charging time of 20 min. After oxidation, the specimens were rinsed in distilled water and dried in air at ambient temperature for 24 h.

### 2.3. Electrophoretic Deposition of Chitosan—Nanosilver Coatings

The electrolytes were prepared by dispersing 1 g of high-weight chitosan (degree of deacetylation > 75%; Sigma Aldrich, St. Louis, MO, United States) and 0.05 g of silver nanopowder (Hongwu International Group Ltd, Guangzhou, China) with an average powder grain about 30 nm in 1 L of 1% acetic acid (Polskie Odczynniki Chemiczne, Gliwice, Poland). Two different electrolytes were used, without (Suspension 1, Specimen A) or with (Suspension 2, Specimens B and C) 1 ml of Tween 20 (Polysorbate 20) (Sigma Aldrich, St. Louis, MO, United States) diluted in 1 L of 1% (v/v) acetic acid. The electrolytes were then homogenized using a magnetic stirrer (at 250 rpm) for 24 h at room temperature. The suspensions were prepared 1 h before deposition. The Ti13Zr13Nb specimen was used as the cathode, and platinum was used as the anode. The electrodes were placed at a distance of 10 mm. A DC power source (MCP/SPN110-01C, Shanghai MCP Corp., Shanghai, China) was applied. The EPD was performed at 10 V (Specimens A and B) and 20 V (Specimen C) for 1 min at room temperature. Finally, the as-deposited composite coatings were rinsed with distilled water and air-dried at room temperature for 48 h. The test variables, their investigated combinations, and further notes are presented in Table 2.

**Table 2.** Test variables, their investigated combinations, and further notes.

Specimen	Properties of Electrophoretic Deposition				
	Chitosan Content (g)	Silver Nanoparticle Content (g)	Polysorbate 20 Content (ml)	Voltage of Deposition (V)	Time of Deposition (min)
	1 L of 1% (v/v) Acetic Acid				
A	1	0.05	-	10	1
B	1	0.05	1	10	1
C	1	0.05	1	20	1

### 2.4. Structure and Morphology of Composite TiO<sub>2</sub>—Chitosan—Nanosilver Coatings

The nanotubular TiO<sub>2</sub> layer and coating surface were examined for each specimen with a high-resolution scanning electron microscope (SEM JEOL JSM- 7800 F, JEOL Ltd., Tokyo, Japan), equipped with a LED detector, at 5 kV acceleration voltage. The chemical compositions of the obtained

coatings were determined using an X-ray energy dispersive spectrometer (EDS) (Edax Inc., Mahwah, NJ, U.S.A.). Specimens with chitosan coatings (A, B, and C) were sputtered with a 10 nm thick layer of gold using a table-top DC magnetron sputtering coater (EM SCD 500, Leica, Vienna, Austria) in pure Ar plasma condition (Argon, Air Products 99.9%) before SEM and EDS techniques were applied. The atomic force microscope (NaniteAFM, Nanosurf AGLiestal, Switzerland) was applied to examine the surface topography. The examinations were carried out in non-contact mode at a force set up at 55 mN. The roughness index Sa was calculated as the mean of several tests made over the area of  $50 \times 50 \mu\text{m}$ . The X-ray diffraction method (XRD) (Phillips X'Pert Pro, Almelo, Netherlands) was applied via a diffractometer (Cu  $K\alpha$ ,  $\lambda = 0.1554 \text{ nm}$ ) in the  $2\theta$  range of  $10\text{--}90^\circ$  at a 0.02 step and 2 s/point, at ambient temperature and under atmospheric pressure. The Fourier-transform infrared (FTIR) spectra were recorded with a spectrophotometer (Perkin Elmer Frontier, Poznań, Poland) at a resolution of  $2 \text{ cm}^{-1}$  in the range of  $400\text{--}4000 \text{ cm}^{-1}$ . For measurements in transmittance mode, the samples were mixed with KBr and pressed to obtain pellets.

### 2.5. Silver Release in Simulated Body Fluid (SBF) Solution

The contents of Ag ions were determined after immersion of specimens A, B, and C in simulated body fluid prepared according to PN-EN ISO 10993-15 by dissolving reagent grade chemicals:  $(\text{NH}_2)_2\text{CO}$  ( $0.13 \text{ gL}^{-1}$ ), NaCl ( $0.7 \text{ gL}^{-1}$ ),  $\text{NaHCO}_3$  ( $1.5 \text{ gL}^{-1}$ ),  $\text{Na}_2\text{HPO}_4$  ( $0.26 \text{ gL}^{-1}$ ),  $\text{K}_2\text{HPO}_4$  ( $0.2 \text{ gL}^{-1}$ ), KSCN ( $0.33 \text{ gL}^{-1}$ ), and KCl ( $1.2 \text{ gL}^{-1}$ ) in 1 L of deionized water. The immersion times were 1, 3, and 7 days at  $39^\circ\text{C}$ . The silver contents were determined using atomic absorption spectrometry (SensAA DUAL, GBC Scientific Equipment Pty Ltd, Australia). A dual-beam optical system with a deuterium lamp was applied for background correction, and a silver hollow cathode lamp (0.4 mA) was the radiation source. The wavelengths used for such analyses were 328.1 and 338.3 nm, and the slit width was 0.5 nm in both cases. To prepare the calibration curve, an Ag basic standard solution with a content of 1000 mg/L in 2%  $\text{HNO}_3$  (VWR Chemicals) was applied. The first standard solutions at a concentration of 10 mg/L were prepared by diluting 1000 mg/L stock solutions. Six subsequent standard solutions were prepared for the calibration curve, at 0.1, 0.3, 0.5, 1.0, 2.0, and 3.0 mg/L. The linear regression method was used to create the calibration curve. The  $R^2$  coefficient was equal to 0.998, which proved acceptable linearity.

### 2.6. Mechanical Studies—Nanoindentation and Nanoscratch Tests

Nanoindentation tests were performed with the NanoTest™ Vantage (NanoTest Vantage, Micro Materials, Wrexham, UK) equipment equipped with a Berkovich three-sided pyramidal diamond. Fifty ( $5 \times 10$ ) independent measurements of nanoindentation for the reference Ti13Zr13Nb sample, Ti13Zr13Nb–TiO<sub>2</sub>, and Ti13Zr13Nb–TiO<sub>2</sub>–chitosan–nanosilver tested specimens (A, B, and C) were carried out. The maximum applied force was 50 mN, the loading and unloading rates were set up at 20 s, and the dwell period at the maximum load was 10 s. The distances between the subsequent indents were 20  $\mu\text{m}$ . During the indent, the load-displacement curve was determined based on the Oliver and Pharr method. Afterward, surface hardness (H) and reduced Young's modulus ( $E_r$ ) were calculated using the integrated software. Estimating Young's modulus (E), Poisson's ratios of 0.33, 0.3, and 0.4 were assumed for the reference Ti13Zr13Nb, Ti13Zr13Nb–TiO<sub>2</sub>, and Ti13Zr13Nb–TiO<sub>2</sub>–chitosan–nanosilver specimens (A, B, and C, respectively).

Nanoscratch tests were made using the same device and the indenter for each specimen. The scratch tests were repeated 10 times while increasing the load from 0 mN to 200 mN at a loading rate of 1.3 mN/s at a distance of 500  $\mu\text{m}$ . The adhesion of the coating was assessed as the stress corresponding to an abrupt change in frictional force during the test.

### 2.7. Contact Angle Studies

The three water contact angle measurements of the reference Ti13Zr13Nb, Ti13Zr13Nb–TiO<sub>2</sub> and Ti13Zr13Nb–TiO<sub>2</sub>–chitosan–nanosilver specimens (A, B, and C) were taken with the contact angle

instrument (Goniometer, Attention Theta Life, Biolin Scientific, Espoo, Finland) at room temperature 10 s after the dropout.

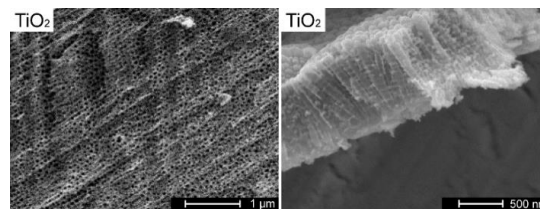
### 2.8. Statistical Analysis

Statistical analysis of the data was performed using a one-way ANOVA (analysis of variance). The Kolmogorov–Smirnov test was used to assess the normal distribution of the data. Statistical significance was set at  $p < 0.05$ . All of the results are presented as the mean  $\pm$  standard deviation (SD).

## 3. Results and Discussion

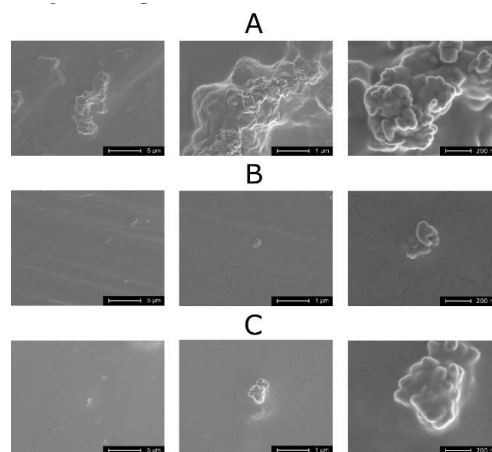
### 3.1. Structure and Morphology of Composite $\text{TiO}_2$ –Chitosan–Nanosilver Coatings

The morphology and cross-section of a nanotubular titanium dioxide layer are presented in Figure 1. The homogeneous layers possessed nanotubes, which were  $0.78 \pm 0.10 \mu\text{m}$  long, about 120 nm in inner diameter, and 25 nm of wall thickness.  $\text{TiO}_2$  nanotubes were aligned vertically and densely packed. The  $\text{TiO}_2$  nanotube layers were previously obtained on a titanium alloy using electrolytes with orthophosphoric acid and hydrofluoric acid [34,35]. Nanotubular titanium dioxide layers designed to ensure better adhesion between the substrate and coatings and for improved corrosion resistance of titanium alloy have also been investigated in the past [36,37].



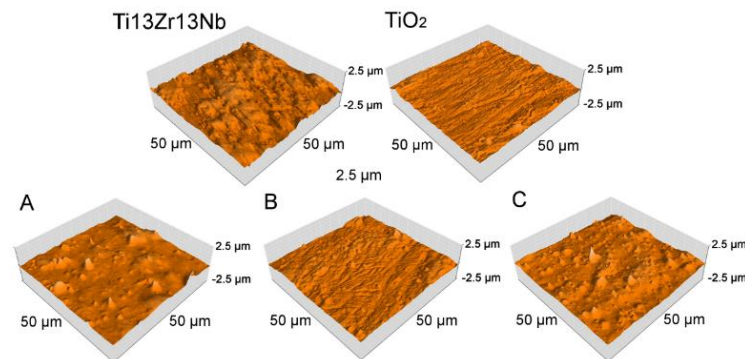
**Figure 1.** Nanotubular dioxide  $\text{TiO}_2$  on the Ti13Zr13Nb alloy (topography—left, thickness—right), Magnifications  $16,000\times$  (on left) and  $32,000\times$  (on right).

Figure 2 shows homogenous chitosan coatings for three nanotubular titanium dioxide specimens produced (regardless of the EPD voltage or electrolyte) on the Ti13Zr13Nb alloy. The micrographs were prepared to examine the dispersion of Ag nanoparticles on chitosan coatings produced in a single process (EPD of chitosan with nanoparticles). For Specimen A (without dispersant in the electrolyte), large agglomerates of nanosilver were obtained (Figure 2A). The presence of dispersant in electrolytes used for the coating of Specimens B (Figure 2B) and C (Figure C) reduced the tendency of nanosilver agglomerates to form. The cracks visible at high magnifications were the result of gold sputtering on samples.



**Figure 2.** Chitosan coatings with nanosilver on the  $\text{TiO}_2$  layer on the Ti13Zr13Nb alloy, Specimens A, B, and C. Magnifications  $1000\times$  (on the left),  $5000\times$  (at the center) and  $25,000\times$  (on the right).

The surface morphology and area roughness of titanium alloy Ti13Zr13Nb, TiO<sub>2</sub> nanotube arrays, and the chitosan-based composite coating, characterized by AFM as 3D images, are shown in Figure 3. The roughness, determined by process parameters, is listed in Table 3.



**Figure 3.** Atomic force microscopy (AFM) topography of the Ti13Zr13Nb substrate, the substrate with the TiO<sub>2</sub> nanotubular layer, Specimens A, B, and C.

**Table 3.** Roughness parameters of the reference specimen, TiO<sub>2</sub> layer, and chitosan composite coatings.

Specimen	Properties	
	Sa Parameter (μm)	Thickness (μm); (mean ± SD; n = 10)
TiO <sub>2</sub> layer on Ti13Zr13Nb alloy	0.07	0.78 ± 0.10
A	0.10	0.78 ± 0.08
B	0.08	0.22 ± 0.04*
C	0.11	3.18 ± 0.18*
reference Ti13Zr13Nb alloy	0.15	-

\* significantly different from Specimen A (analysis of variance (ANOVA)  $p < 0.05$ )

A significant change in surface topography occurred following the anodization and electrophoretic deposition of the composite chitosan coatings. The addition of polysorbate 20 made the roughness lower because it is a compound that decreases surface tension and thus enhances the formation of the homogenous layer. An increase in voltage resulted in a small increase in the roughness and a 4-fold increase in coating thickness caused by the increasing amount of particles delivered to the surface in a time unit, always associated with a tendency to create thick and more porous layers. Moreover, the experiments confirmed that an increase of applied voltage caused the formation of more bubbles in chitosan coatings, which was the result of water hydrolysis during the EPD process and hydrogen evolution at the deposition electrode [38]. Higher voltage increases the intensity of this process, which results in more porous coatings [39]. The thickness of the composite coating was negatively influenced by the addition of polysorbate 20, which could be attributed to closer packing of particles (lower roughness). The presence of TiO<sub>2</sub> decreased the surface roughness due to the surface preparation before anodizing. Even on an unpolished surface with a high roughness parameter (0.15 μm), titanium dioxide was formed at the same rate across the entire surface, which thus created a homogenous layer and decreased the surface's roughness.

The thickness values of the chitosan composite layers are shown in Figure 4 and presented in Table 3. The thickness of the coatings correlated with the results shown in SEM images (Figure 2) and AFM topographies (Figure 3). The nanotubular titanium dioxide layer was distinctly observed under the thinnest chitosan coating by both SEM and AFM (Specimen B). The presence of polysorbate 20 for specimens obtained at 10 V decreased the thickness of the layer (Specimens A and B).

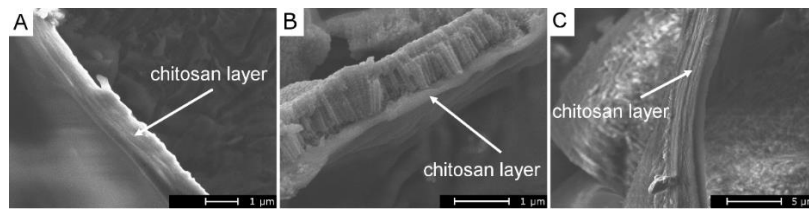


**Figure 4.** Chitosan composite coatings on  $\text{TiO}_2$  on  $\text{Ti}_{13}\text{Zr}_{13}\text{Nb}$ . Three different parts of chitosan coating are shown in subfigures; arrows indicate one of the coating interfaces.

Figures 5 and 6 show the elemental distribution map and chemical composition of selected areas for Specimens A and B. The EDS map for Specimen A, shown in Figure 5, confirmed the occurrence of agglomerates of silver nanoparticles larger than those found in Specimen B. The EDS map for Specimen B, shown in Figure 6, proved an improved dispersion of silver nanoparticles following the use of dispersant (polysorbate 20) and, consequently, the appearance of a larger specific surface area with silver nanoparticles. For both specimens, A in Figure 5 and B in Figure 6, mapping Ti and O elements revealed a uniform distribution of nanotubular titanium dioxide on the  $\text{Ti}_{13}\text{Zr}_{13}\text{Nb}$  alloy.

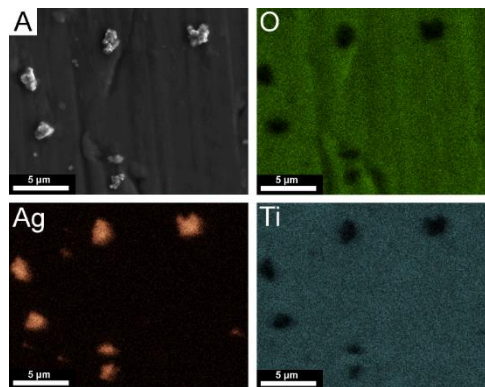


**Figure 5.** Elemental distribution map and chemical composition from a selected area, Specimen A.

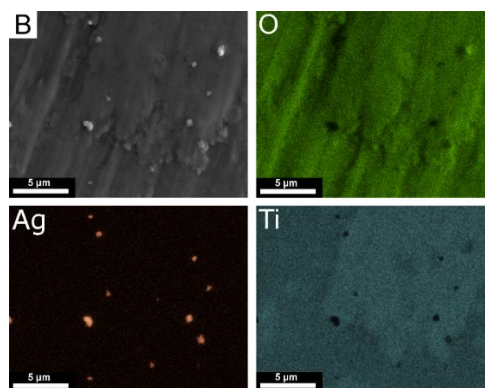


**Figure 6.** Elemental distribution map and chemical composition from a chosen region, Specimen B.

EDS mapping required collection of a stable image over about 30 min, which proved to be impossible for Specimen C. This was caused by the excessive thickness of the chitosan layer which, being an electrical insulator, resulted in image drift (a blurred image) during the EDS mapping, despite the sputtering of the gold layer. The highest content and more dispersed silver nanoparticles on Specimen B resulted in a more prolonged silver release to the surrounding implant tissue and, in consequence, a more effective bactericidal effect of these particles. The formation of agglomerates of silver nanoparticles has been previously reported [40,41]. The adverse impact of silver particles'

agglomeration on antimicrobial behavior has been explained as being due to decreasing contact between nanoparticles and bacterial cells. Silver nanoparticle agglomeration reduces their antibacterial effects and inhibits the release of silver ions, as the agglomerates have a lower surface-to-volume ratio and lower contact possibility with bacteria in comparison to nanoparticles. The problem of silver nanoparticle agglomeration may be solved by adding dispersing agents like polysorbate 20 to their suspension, which stabilizes Ag nanoparticles by enhancing the electrostatic repulsive forces between them.

The X-ray diffractograms of the tested specimens are depicted in Figure 7. In each of them, peaks can be observed that can be attributed to the Ti<sub>13</sub>Zr<sub>13</sub>Nb substrate (Figure 7) [42]. For the sample with the TiO<sub>2</sub> nanotubular layer, the difference in relative intensities of the primary phases (support) of peaks at the 2 $\theta$  range of 35–42° may have been linked to the formation of the layer visible in the SEM and AFM micrographs (Figures 1 and 3, respectively).

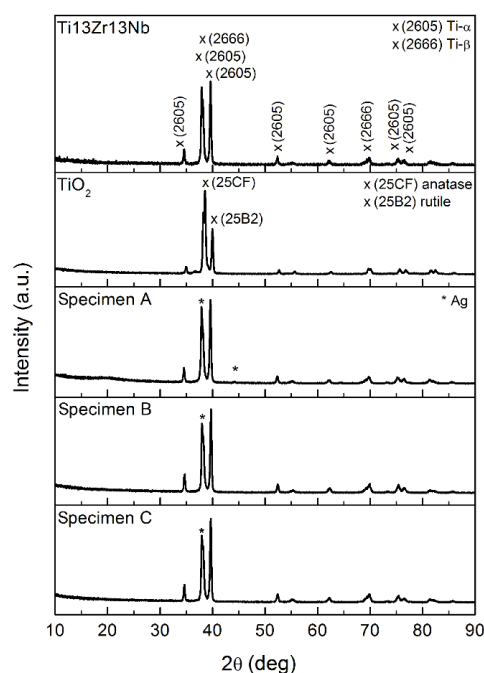


**Figure 7.** X-ray diffractogram of the Ti<sub>13</sub>Zr<sub>13</sub>Nb substrate, and the substrate with the TiO<sub>2</sub> nanotube layer, Specimens A, B, and C. The peak intensities are normalized.

Due to the overlapping of peaks, the crystalline structure of the titania nanotubes could not be determined. Similar results were reported previously for nanotube layers formed on pure titanium via anodization, where nanotube arrays of mixed-phase rutile and anatase were developed [43]. In the samples with the chitosan–nanosilver layer, the standard for amorphous chitosan broad maximum could be identified only for specimen A ( $2\theta = 15\text{--}25^\circ$ ); however, its relative (to main phase peaks) intensity was very low [44]. The visible peaks ( $2\theta = 38$  and  $44^\circ$ ) were attributed to the cubic crystalline structure of silver (ICDD 01-087-0717). Nevertheless, due to low concentration and nanocrystallinity, their intensity was very low. The main peak of the nanosilver phase overlapped with the support material peaks.

Figure 8 demonstrates the FTIR spectra of the investigated materials. A clear spectrum of chitosan was observed for Specimen C, with the most pronounced chitosan layer. The measured spectrum corresponded to other results on stand-alone and composite chitosan from the literature [45–49]. The main bands appearing in that spectrum were due to stretching vibrations of OH groups in the range from  $3750\text{ cm}^{-1}$  to  $3000\text{ cm}^{-1}$ , which overlapped with the stretching vibration of N–H and the C–H bond in  $-\text{CH}_2$  and  $-\text{CH}_3$  groups, respectively [45,50]. Bending vibrations of methylene and methyl groups were visible at  $1375\text{--}1430\text{ cm}^{-1}$  [51]. Absorption in the range of  $1680\text{--}1480\text{ cm}^{-1}$  was associated

with the vibrations of carbonyl bonds (C=O) of the amide groups [52], and absorption from  $1160\text{ cm}^{-1}$  to  $1000\text{ cm}^{-1}$  was associated with vibrations of CO [48]. The band located at around  $1150\text{ cm}^{-1}$  was related to asymmetrical vibrations of CO in the oxygen bridge resulting from the deacetylation of chitosan, and the bands near  $1080\text{--}1025\text{ cm}^{-1}$  were associated with C-O stretching [48]. The small peak at  $\sim 890\text{ cm}^{-1}$  corresponded to the wagging of the saccharide structure of chitosan [46].

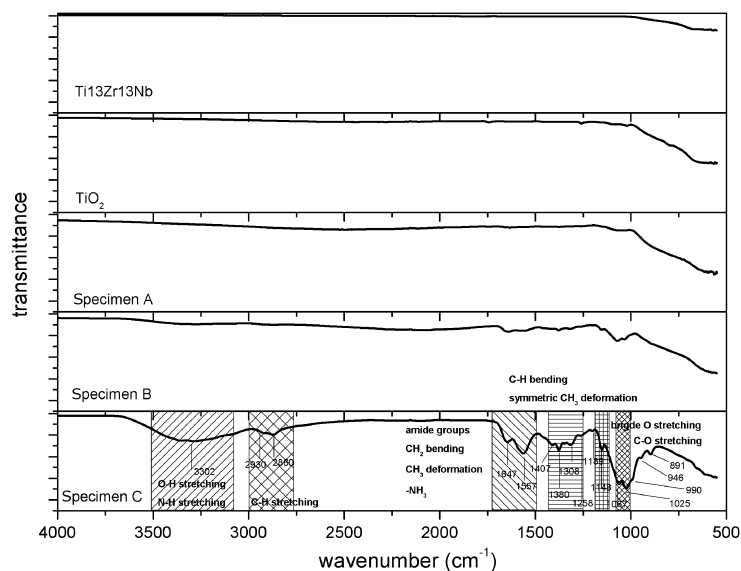


**Figure 8.** Fourier-transform infrared (FTIR) spectra of the Ti13Zr13Nb substrate and the substrate with the TiO<sub>2</sub> nanotube layers: Specimen A, Specimen B, and Specimen C.

### 3.2. Silver Release in Simulated Body Fluid (SBF) Solution

Ag total contents in solutions to which the specimens were exposed are presented in Figure 9. It was noted when the time of specimen exposure increased, the Ag concentration increased. Taking into account the calculated deviations of measured values, the increase in Ag content in solutions was  $0.013\text{--}0.036\text{ mg/L}$  per day of exposure. The mean value of the increase of the Ag concentration can thus be expressed as an average of  $0.025\text{ mg/L}$  per day of exposure, providing proof of the process of slow transport of Ag ions from tested materials to SBF.

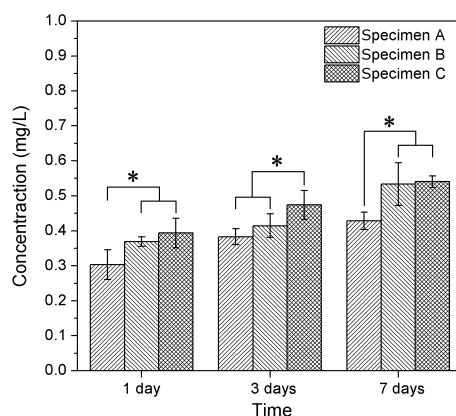


**Figure 9.** Cumulative concentrations of Ag ions released from chitosan composite coatings deposited on the nanotubular layer after 1, 3, and 7 days exposure in simulated body fluid (SBF) at  $39\text{ }^{\circ}\text{C}$ . Data are presented as the mean  $\pm$  SD ( $n = 4$ ). \*  $p < 0.05$ ; one-way ANOVA with Bonferroni post hoc correction.

Nowadays, postoperative infection is one of the main problems in orthopedic surgeries. The bactericidal properties of 35 ppb silver have been reported [53], and the most biofilm-forming

bacteria are found on the surface of implants [54]. Positive effects of released silver particles were observed for all tested specimens after 1 day when the risk of bacterial inflammation could be the highest. The slow release of silver nanoparticles into the SBF may have been caused by the presence of numerous hydroxyl and amine groups with a strong affinity to metallic elements such as silver [55]. A local increase in Ag content within the adjacent tissues in a human body will thus occur and prevent possible local inflammation states, which, consequently, will ensure long-term antibacterial protection. Moreover, the reference dose for allowable oral exposure of Ag, as defined by the US EPA (United States Environmental Protection Agency) is 0.005 mg of Ag/kg of body mass per day and, considering the maximum Ag release rate determined here, the maximum daily allowable consumption of Ag will not be exceeded in an average adult [56].

Bacterial inactivation may occur via two different actions: at the direct contact of bacteria with nanosilver at the interface or by the interaction of bacteria and the silver ions that appear during the dissolution of nanosilver [57–59]. The present results did not support either hypothesis, but the direct contact of silver ions and bacteria in solution seems more probable, as the antibacterial efficiency followed the silver release. Additionally, more bacteria could be present in solution than at the silver–solution interface, and more precisely at the surface of the nanosilver aggregates.

### 3.3. Mechanical Studies—Nanoindentation and Nanoscratch Tests

The results of the nanoindentation test are shown in Figure 10. Typical nanoindentation properties such as hardness, Young’s modulus, maximum depth, plastic and elastic work, and  $H^3/E^2$  factor were investigated. The remarkable standard deviations were characteristic of nanoindentation. For all of the Ti13Zr13Nb titanium surface modifications, decreasing nanohardness, Young’s modulus, and  $H^3/E^2$  factors were observed compared to the reference Ti13Zr13Nb alloy. The research proved a significant difference between Specimens A and B, and Specimens A and C for all studied nanoindentation properties.

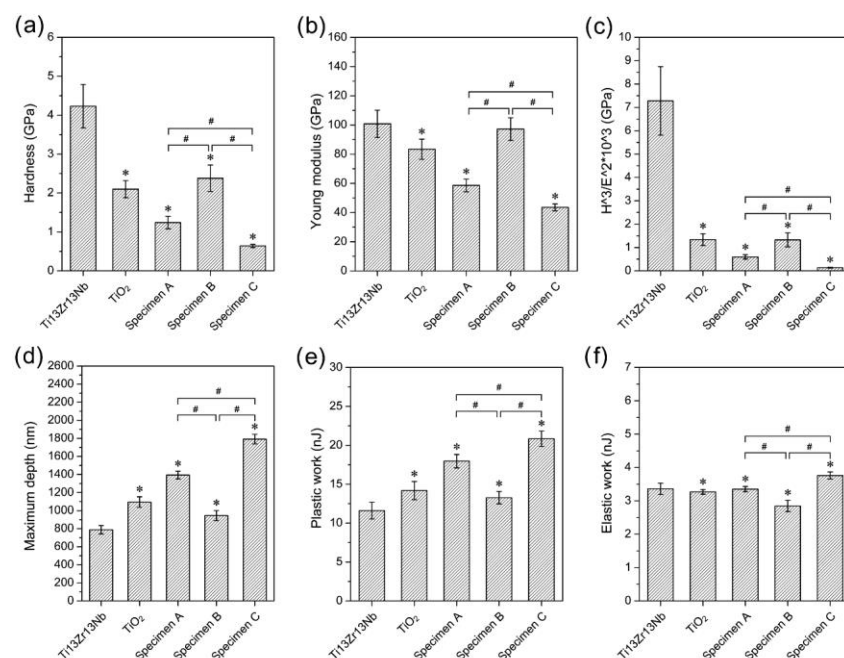


**Figure 10.** Nanomechanical properties: (a) hardness, (b) Young modulus, and (c)  $H^3/E^2$ ; nanoindentation properties: (d) maximum depth, (e) plastic work, and (f) elastic work for Ti13Zr13Nb substrate, substrate with the TiO<sub>2</sub> nanotube layer, Specimen A, Specimen B, and Specimen C. Data are presented as the mean  $\pm$  SD ( $n = 50$ ). A significant difference was observed between the Ti13Zr13Nb control specimen (ANOVA with Bonferroni post hoc correction  $*p < 0.05$ ) and Specimens A, B, and C (ANOVA with Bonferroni post hoc correction  $\#p < 0.05$ ).

The  $H^3/E^2$  factor was calculated using the results for the nanoindentation test. The  $H^3/E^2$  factor describes the resistance of a material to plastic deformation [60]. The deposition of composite coatings on the nanotubular layer caused a decrease in hardness and Young's modulus, except when a simultaneous deposition was made in the presence of a surface-active compound at a lower voltage value. This was assumed to be an effect of the close packing and high density of coatings obtained under such conditions. Mechanical properties such as hardness and Young's modulus are one of the most essential features for long-term and load-bearing implants. It has been proven that a significant difference between the properties of human bone and an implant can cause the "shielding effect" and, in consequence, a danger of loosening the implant [61]. The hardness and Young's modulus of Ti13Zr13Nb decreased after anodization, as reported previously by Chernozem et al. [60] and Crawford et al. [62]. A value of Young's modulus close to that of human bone (10–30 GPa) was obtained for Specimen C, characterized by the lowest nanohardness and  $E^3/H^2$  factor value [33]. It was expected that the specimens coated with chitosan (A, B, and C) would be characterized by lower nanomechanical properties than the Ti13Zr13Nb alloy and Ti13Zr13Nb after the anodization process, but, because of the small thickness of the chitosan coatings on Specimen B (about 0.22  $\mu\text{m}$ ), nanomechanical tests for this specimen probably involved to a significant extent the TiO<sub>2</sub> layer under the coating. This fact was confirmed by the lack of considerable difference between the nanohardness and Young's modulus values of the TiO<sub>2</sub> layer and Specimen B.

The results of the nanoscratch studies are shown in Table 4. The addition of the surface-active substance did not influence critical friction, but significantly decreased the load representative of the delamination force of the layers/coatings.

**Table 4.** Nanoscratch test properties of the TiO<sub>2</sub> layer and chitosan composite coatings (mean  $\pm$  SD;  $n = 10$ ).

Specimen	Nanoscratch Test Properties	
	Critical Friction (mN)	Critical Load (mN)
TiO <sub>2</sub> layer on Ti13Zr13Nb alloy	58.22 $\pm$ 20.43	85.95 $\pm$ 28.00
A	100.72 $\pm$ 9.31*	152.59 $\pm$ 13.93*
B	101.58 $\pm$ 41.76*	79.91 $\pm$ 25.44#
C	106.65 $\pm$ 28.97*	85.48 $\pm$ 30.34#

\* significantly different from TiO<sub>2</sub> layer on Ti13Zr13Nb alloy (ANOVA  $p < 0.05$ ). # significantly different from Specimen A (ANOVA  $p < 0.05$ ).

The highest adhesion to the bare surface was revealed for Specimen A. Values of the critical force were increased almost 2-fold for specimens with chitosan layers on TiO<sub>2</sub> compared with a single TiO<sub>2</sub> layer. Nowadays, the nanoscratch technique is preferred for determining the adhesion of thin layers and coatings [63–66]. The layers and coatings for implants should possess high adhesion to metallic substrates, in particular against shear stresses, and the nanoscratch test used here allows such expectations to be assessed. Unfortunately, to date, there has been almost no research conducted on the use of this technique on chitosan coatings. However, Tozar [67,68] determined only a friction coefficient in the nanoscratch sliding test as well as hardness and Young's modulus in the nanoindentation test for chitosan–hydroxyapatite–collagen coatings.

### 3.4. Measurements of the Contact Angle

The wettability of all specimens was in the range of values characteristic of high biocompatibility (Figure 11), which confirmed the hydrophilic character of the investigated surfaces ( $\theta < 90^\circ$ ). The wettability of a surface is crucial for cell attachment [38]. The recommended contact angle values needed for the best attachment to cells for bone replacement implants are 35–85°, and the optimal value is 55° [69]. All investigated surfaces fulfilled this criterion. Moreover, Specimens B and C are closest to the optimum contact angle value.

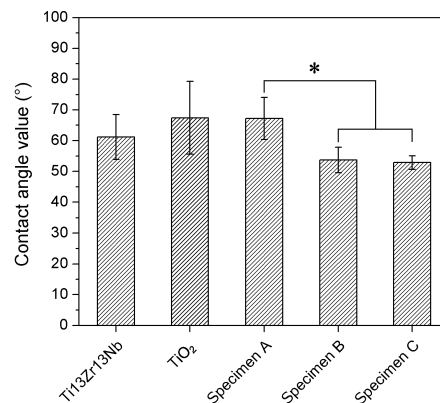


**Figure 11.** Water contact angle at room temperature for the reference non-coated specimen, TiO<sub>2</sub> layer, and chitosan composite coatings. Data are presented as the mean  $\pm$  SD ( $n = 3$ ). \*  $p < 0.05$ ; one-way ANOVA with Bonferroni post hoc correction.

The differences observed between uncoated and coated specimens, and for each coating, were tiny or fell within the standard deviations. The addition of the surface-active substance somewhat increased the wettability, but no explanation for this was found. The most likely reason is that the presence of polysorbate 20 in the chitosan coatings decreased the surface tension for Specimens B and C, as suggested by Ziani et al. [31], who applied Tween 20 as a surface-active substance. As a consequence, the decrease of the surface tension increased the water contact angle (Specimen B and C), which was a consequence of the presence of silver nanoparticles in specimens B and C provided that they were not agglomerated. Similar results have been previously reported [70]. Agglomeration of silver nanoparticles (as for Specimen A) resulted in an increase of hydrophobicity and contact angle in comparison to well-dispersed nanoparticles.

#### 4. Conclusions

Chitosan–nanosilver coatings were deposited on the nanotubular oxide layer of Ti13Zr13Nb alloy using the electrophoretic technique. The coatings were, at the applied solution and process parameters, homogeneous and well adjacent to the base, and demonstrated slow dissolution of nanosilver into the simulated body fluid.

The addition of a surface-active compound resulted in a small decrease in roughness, an increase in nanohardness, faster liberation of silver ions, and a reduction of critical load in a scratch test of tested composite coatings, which was attributed to a smoother and more packed (less porous) surface.

The increase in EPD voltage caused a high increase in coating thickness, a decrease in hardness, faster dissolution of nanosilver, and a small increase in the critical load and friction force of tested coatings.

The best process deposition parameters for the tested composite chitosan–nanosilver coating, the nanotubular oxide layer, and the Ti13Zr13Nb alloy as a substrate, used as an electrolyte 1 g/L of high-weight chitosan with a degree of deacetylation  $> 75\%$ , 0.05 g/L of nanosilver with an average particle size of about 30 nm, and 1 ml/L of Tween 20 (polysorbate 20) solution in 1% aqueous acetic acid; EPD voltage 10 V and time 1 min at room temperature.

**Author Contributions:** Conceptualization, M.B., and Ł.P.; methodology, M.B., Ł.P., A.M.-G., G.S., and B.C.; formal analysis, M.B., Ł.P., A.M.-G. and A.Z.; investigation, M.B., Ł.P., A.M.-G., G.S., and B.C.; writing—original draft preparation, M.B., and A.Z.; writing—review and editing, M.B. and A.Z.; supervision, M.B., and A.Z. All authors have read and agreed to the published version of the manuscript.

**Funding:** This research received no external funding.

**Conflicts of Interest:** The authors declare no conflict of interest.

## References

1. Dinu, M.; Franchi, S.; Pruna, V.; Cotrut, C.M.; Secchi, V.; Santi, M.; Titorencu, I.; Battocchio, C.; Iucci, G.; Vladescu, A. Ti-Nb-Zr system and its surface biofunctionalization for biomedical applications. In *Titanium in Medical and Dental Applications*; Froes, F.H., Qian, M., Eds.; Woodhead Publishing Series in Biomaterials; Woodhead Publishing: Cambridge, UK, 2018; pp. 175–200. ISBN 978-0-12-812456-7.
2. Ferraris, S.; Spriano, S. Antibacterial titanium surfaces for medical implants. *Mater. Sci. Eng. C* **2016**, *61*, 965–978. [[CrossRef](#)] [[PubMed](#)]
3. Piątkowski, M.; Radwan-Pragłowska, J.; Janus, Ł.; Bogdał, D.; Matysek, D.; Cablik, V. Microwave-assisted synthesis and characterization of chitosan aerogels doped with Au-NPs for skin regeneration. *Polym. Test.* **2019**, *73*, 366–376. [[CrossRef](#)]
4. Möhler, J.S.; Sim, W.; Blaskovich, M.A.T.; Cooper, M.A.; Ziora, Z.M. Silver bullets: A new lustre on an old antimicrobial agent. *Biotechnol. Adv.* **2018**, *36*, 1391–1411. [[CrossRef](#)] [[PubMed](#)]
5. Wekwejt, M.; Moritz, N.; Świeczko-Żurek, B.; Pałubicka, A. Biomechanical testing of bioactive bone cements—A comparison of the impact of modifiers: Antibiotics and nanometals. *Polym. Test.* **2018**, *70*, 234–243. [[CrossRef](#)]
6. Volova, T.G.; Shumilova, A.A.; Shidlovskiy, I.P.; Nikolaeva, E.D.; Sukovatiy, A.G.; Vasiliev, A.D.; Shishatskaya, E.I. Antibacterial properties of films of cellulose composites with silver nanoparticles and antibiotics. *Polym. Test.* **2018**, *65*, 54–68. [[CrossRef](#)]
7. Zheng, K.; Setyawati, M.I.; Leong, D.T.; Xie, J. Antimicrobial silver nanomaterials. *Coord. Chem. Rev.* **2018**, *357*, 1–17. [[CrossRef](#)]
8. Gilabert-Chirivella, E.; Pérez-Feito, R.; Ribeiro, C.; Ribeiro, S.; Correia, D.M.; González-Martín, M.L.; Manero, J.M.; Lanceros-Méndez, S.; Ferrer, G.G.; Gómez-Ribelles, J.L. Chitosan patterning on titanium implants. *Prog. Org. Coat.* **2017**, *111*, 23–28. [[CrossRef](#)]
9. Sani, I.K.; Pirsá, S.; Tağı, Ş. Preparation of chitosan/zinc oxide/Melissa officinalis essential oil nano-composite film and evaluation of physical, mechanical and antimicrobial properties by response surface method. *Polym. Test.* **2019**, *79*, 106004. [[CrossRef](#)]
10. Urbanek, O.; Sajkiewicz, P.; Pierini, F. The effect of polarity in the electrospinning process on PCL/chitosan nanofibres' structure, properties and efficiency of surface modification. *Polymer* **2017**, *124*, 168–175. [[CrossRef](#)]
11. Muxika, A.; Etxabide, A.; Uranga, J.; Guerrero, P.; de la Caba, K. Chitosan as a bioactive polymer: Processing, properties and applications. *Int. J. Biol. Macromol.* **2017**, *105*, 1358–1368. [[CrossRef](#)]
12. Olad, A.; Hagh, H.B.K. Graphene oxide and amin-modified graphene oxide incorporated chitosan-gelatin scaffolds as promising materials for tissue engineering. *Compos. Part B Eng.* **2019**, *162*, 692–702. [[CrossRef](#)]
13. Divakar, D.D.; Jastaniyah, N.T.; Altamimi, H.G.; Alnakhli, Y.O.; Muzaheed; Alkheraif, A.A.; Haleem, S. Enhanced antimicrobial activity of naturally derived bioactive molecule chitosan conjugated silver nanoparticle against dental implant pathogens. *Int. J. Biol. Macromol.* **2018**, *108*, 790–797. [[CrossRef](#)] [[PubMed](#)]
14. Praxedes, A.P.P.; Webler, G.D.; Souza, S.T.; Ribeiro, A.S.; Fonseca, E.J.S.; Oliveira, I.N. De Non-monotonic wetting behavior of chitosan films induced by silver nanoparticles. *Appl. Surf. Sci.* **2016**, *370*, 25–31. [[CrossRef](#)]
15. Yan, Y.; Zhang, X.; Li, C.; Huang, Y.; Ding, Q.; Pang, X. Preparation and characterization of chitosan-silver/hydroxyapatite composite coatings on TiO<sub>2</sub> nanotube for biomedical applications. *Appl. Surf. Sci.* **2015**, *332*, 62–69. [[CrossRef](#)]
16. Jennings, J.A.; Velasquez Pulgarin, D.A.; Kunwar, D.L.; Babu, J.; Mishra, S.; Bumgardner, J. Bacterial inhibition by chitosan coatings loaded with silver-decorated calcium phosphate microspheres. *Thin Solid Film.* **2015**, *596*, 83–86. [[CrossRef](#)]
17. Kishore, R.; Awasthi, S.; Dhayalan, A.; Ferreira, J.M.F.; Kannan, S. Deposition, structure, physical and in-vitro characteristics of Ag-doped  $\beta$ -Ca<sub>3</sub>(PO<sub>4</sub>)<sub>2</sub>/chitosan hybrid composite coatings on Titanium metal. *Mater. Sci. Eng. C* **2016**, *62*, 692–701.
18. Lin, S.; Chen, L.; Huang, L.; Cao, S.; Luo, X.; Liu, K. Novel antimicrobial chitosan-cellulose composite films bioconjugated with silver nanoparticles. *Ind. Crops Prod.* **2015**, *70*, 395–403. [[CrossRef](#)]
19. Mishra, S.K.; Ferreira, J.M.F.; Kannan, S. Mechanically stable antimicrobial chitosan-PVA-silver nanocomposite coatings deposited on titanium implants. *Carbohydr. Polym.* **2015**, *121*, 37–48. [[CrossRef](#)]

20. Wang, Y.; Guo, X.; Pan, R.; Han, D.; Chen, T.; Geng, Z.; Xiong, Y.; Chen, Y. Electrodeposition of chitosan/gelatin/nanosilver: A new method for constructing biopolymer/nanoparticle composite films with conductivity and antibacterial activity. *Mater. Sci. Eng. C* **2015**, *53*, 222–228. [[CrossRef](#)]
21. Arjunan, N.; Kumari, H.L.J.; Singaravelu, C.M.; Kandasamy, R.; Kandasamy, J. Physicochemical investigations of biogenic chitosan-silver nanocomposite as antimicrobial and anticancer agent. *Int. J. Biol. Macromol.* **2016**, *92*, 77–87. [[CrossRef](#)]
22. Dananjaya, S.H.S.; Erandani, W.K.C.U.; Kim, C.H.; Nikapitiya, C.; Lee, J.; De Zoysa, M. Comparative study on antifungal activities of chitosan nanoparticles and chitosan silver nano composites against *Fusarium oxysporum* species complex. *Int. J. Biol. Macromol.* **2017**, *105*, 478–488. [[CrossRef](#)] [[PubMed](#)]
23. Kalaivani, R.; Maruthupandy, M.; Muneeswaran, T.; Hameedha Beevi, A.; Anand, M.; Ramakritinan, C.M.; Kumaraguru, A.K. Synthesis of chitosan mediated silver nanoparticles (Ag NPs) for potential antimicrobial applications. *Front. Lab. Med.* **2018**, *2*, 30–35. [[CrossRef](#)]
24. Wongpreecha, J.; Polpanich, D.; Suteewong, T.; Kaewsaneha, C. One-pot, large-scale green synthesis of silver nanoparticles-chitosan with enhanced antibacterial activity and low cytotoxicity. *Carbohydr. Polym.* **2018**, *199*, 641–648. [[CrossRef](#)] [[PubMed](#)]
25. Xie, Y.; Liao, X.; Zhang, J.; Yang, F.; Fan, Z. Novel chitosan hydrogels reinforced by silver nanoparticles with ultrahigh mechanical and high antibacterial properties for accelerating wound healing. *Int. J. Biol. Macromol.* **2018**, *119*, 402–412. [[CrossRef](#)]
26. Rinaldi, F.; Del Favero, E.; Moeller, J.; Hanieh, P.N.; Passeri, D.; Rossi, M.; Angeloni, L.; Venditti, I.; Marianecchi, C.; Carafa, M.; et al. Hydrophilic silver nanoparticles loaded into niosomes: Physical-chemical characterization in view of biological applications. *Nanomaterials* **2019**, *9*, 1177. [[CrossRef](#)]
27. Li, X.; Lenhart, J.J.; Walker, H.W. Aggregation kinetics and dissolution of coated silver nanoparticles. *Langmuir* **2012**, *28*, 1095–1104. [[CrossRef](#)]
28. Cavalieri, F.; Tortora, M.; Stringaro, A.; Colone, M.; Baldassarri, L. Nanomedicines for antimicrobial interventions. *J. Hosp. Infect.* **2014**, *88*, 183–190. [[CrossRef](#)]
29. Badawy, M.E.I.; Lotfy, T.M.R.; Shawir, S.M.S. Preparation and antibacterial activity of chitosan-silver nanoparticles for application in preservation of minced meat. *Bull. Natl. Res. Cent.* **2019**, *43*, 83. [[CrossRef](#)]
30. Chowdappa, P.; Shivakumar, G.; Chethana, C.S.; Madhur, S. Antifungal activity of chitosan-silver nanoparticle composite against *Colletotrichum gloeosporioides* associated with mango anthracnose. *Afr. J. Microbiol. Res.* **2014**, *8*, 1803–1812.
31. Ziani, K.; Oses, J.; Coma, V.; Maté, J.I. Effect of the presence of glycerol and Tween 20 on the chemical and physical properties of films based on chitosan with different degree of deacetylation. *LWT Food Sci. Technol.* **2008**, *41*, 2159–2165. [[CrossRef](#)]
32. Casariego, A.; Souza, B.W.S.; Vicente, A.A.; Teixeira, J.A.; Cruz, L.; Díaz, R. Chitosan coating surface properties as affected by plasticizer, surfactant and polymer concentrations in relation to the surface properties of tomato and carrot. *Food Hydrocoll.* **2008**, *22*, 1452–1459. [[CrossRef](#)]
33. Mohan, L.; Durgalakshmi, D.; Geetha, M.; Sankara Narayanan, T.S.N.; Asokamani, R. Electrophoretic deposition of nanocomposite (HAp + TiO<sub>2</sub>) on titanium alloy for biomedical applications. *Ceram. Int.* **2012**, *38*, 3435–3443. [[CrossRef](#)]
34. Kodama, A.; Bauer, S.; Komatsu, A.; Asoh, H.; Ono, S.; Schmuki, P. Bioactivation of titanium surfaces using coatings of TiO<sub>2</sub> nanotubes rapidly pre-loaded with synthetic hydroxyapatite. *Acta Biomater.* **2009**, *5*, 2322–2330. [[CrossRef](#)] [[PubMed](#)]
35. Ossowska, A.; Sobieszczyk, S.; Supernak, M.; Zielinski, A. Morphology and properties of nanotubular oxide layer on the “Ti-13Zr-13Nb” alloy. *Surf. Coat. Technol.* **2014**, *258*, 1239–1248. [[CrossRef](#)]
36. Zielinski, A.; Antoniuk, P.; Krzysztofowicz, K. Nanotubular oxide layers and hydroxyapatite coatings on “Ti-13Zr013Nb” alloy. *Surf. Sci.* **2014**, *30*, 643–649.
37. Chrzanowski, W.; Szewczenko, J.; Tyrlik-Held, J.; Marciniak, J.; Zak, J. Influence of the anodic oxidation on the physicochemical properties of the Ti6Al4V ELI alloy. *J. Mater. Process. Technol.* **2005**, *162–163*, 163–168. [[CrossRef](#)]
38. Gebhardt, F.; Seuss, S.; Turhan, M.C.; Hornberger, H.; Virtanen, S.; Boccaccini, A.R. Characterization of electrophoretic chitosan coatings on stainless steel. *Mater. Lett.* **2012**, *66*, 302–304. [[CrossRef](#)]
39. Pang, X.; Zhitomirsky, I. Electrophoretic deposition of composite hydroxyapatite-chitosan coatings. *Mater. Charact.* **2007**, *58*, 339–348. [[CrossRef](#)]

40. Guo, L.; Yuan, W.; Lu, Z.; Li, C.M. Polymer/nanosilver composite coatings for antibacterial applications. *Colloids Surf. A Physicochem. Eng. Asp.* **2013**, *439*, 69–83. [[CrossRef](#)]
41. Li, Y.; Zhang, W.; Niu, J.; Chen, Y. Surface-coating-dependent dissolution, aggregation, and reactive oxygen species (ROS) generation of silver nanoparticles under different irradiation conditions. *Environ. Sci. Technol.* **2013**, *47*, 10293–10301. [[CrossRef](#)]
42. Ozaltin, K.; Panigrahi, A.; Chrominski, W.; Bulutsuz, A.G.; Kulczyk, M.; Zehetbauer, M.J.; Lewandowska, M. Microstructure and Texture Evolutions of Biomedical Ti-13Nb-13Zr Alloy Processed by Hydrostatic Extrusion. *Metall. Mater. Trans. A Phys. Metall. Mater. Sci.* **2017**, *48*, 5747–5755. [[CrossRef](#)]
43. Goodarzi, S.; Moztarzadeh, F.; Nezafati, N.; Omidvar, H. Titanium dioxide nanotube arrays: A novel approach into periodontal tissue regeneration on the surface of titanium implants. *Adv. Mater. Lett.* **2016**, *7*, 209–215. [[CrossRef](#)]
44. Kumar, S.; Koh, J. Physicochemical and optical study of chitosan-terephthaldehyde derivative for biomedical applications. *Int. J. Biol. Macromol.* **2012**, *51*, 1167–1172. [[CrossRef](#)] [[PubMed](#)]
45. Rieppo, J.; Rieppo, L.; Saarakkala, S.; Jurvelin, J.S. Fourier Transform Infrared Imaging Spectroscopy in Biomedicine-Important Things to Consider When Planning a New Experiment. In *Fourier Transforms-New Analytical Approaches and FTIR Strategies*; Nikolic, G., Ed.; Intech Open: London, UK, 2011; pp. 1–14.
46. Paluszkiwicz, C.; Stodolak, E.; Hasik, M.; Blazewicz, M. FT-IR study of montmorillonite–chitosan nanocomposite materials. *Spectrochim. Acta Part A Mol. Biomol. Spectrosc.* **2011**, *79*, 784–788. [[CrossRef](#)] [[PubMed](#)]
47. Corazzari, I.; Nisticò, R.; Turci, F.; Faga, M.; Franzoso, F.; Tabasso, S.; Magnacca, G. Advanced physico-chemical characterization of chitosan by means of TGA coupled on-line with FTIR and GCMS: Thermal degradation and water adsorption capacity. *Polym. Degrad. Stab.* **2014**, *112*, 1–9. [[CrossRef](#)]
48. Dimzon, I.K.D.; Knepper, T.P. International Journal of Biological Macromolecules Degree of deacetylation of chitosan by infrared spectroscopy and partial least squares. *Int. J. Biol. Macromol.* **2015**, *72*, 939–945. [[CrossRef](#)]
49. Silva, S.M.L.; Braga, C.R.C.; Fook, M.V.L.; Raposo, C.M.O.; Carvalho, L.H.; Canedo, E.L. Application of Infrared Spectroscopy to Analysis of Chitosan/Clay Nanocomposites. In *Infrared Spectroscopy*; Theophanides, T., Ed.; IntechOpen: Rijeka, Croatia, 2012.
50. Fan, M.; Dai, D.; Huang, B. Fourier Transform Infrared Spectroscopy for Natural Fibres. In *Fourier Transform*; Salih, S.M., Ed.; IntechOpen: Rijeka, Croatia, 2012.
51. Mano, J.F.; Koniarova, D.; Reis, R.L. Thermal properties of thermoplastic starch/synthetic polymer blends with potential biomedical applicability. *J. Mater. Sci. Mater. Med.* **2003**, *14*, 127–135. [[CrossRef](#)]
52. Marchessault, R.H.; Ravenelle, F.; Zhu, X.X. (Eds.) *Polysaccharides for Drug Delivery and Pharmaceutical Applications*; ACS Symposium Series; American Chemical Society: Washington, DC, USA, 2006; Volume 934, ISBN 0-8412-3960-6.
53. Geng, Z.; Wang, R.; Zhuo, X.; Li, Z.; Huang, Y.; Ma, L.; Cui, Z.; Zhu, S.; Liang, Y.; Liu, Y.; et al. Incorporation of silver and strontium in hydroxyapatite coating on titanium surface for enhanced antibacterial and biological properties. *Mater. Sci. Eng. C* **2017**, *71*, 852–861. [[CrossRef](#)]
54. Jayaprakash, N.; Judith Vijaya, J.; John Kennedy, L.; Priadharsini, K.; Palani, P.; Louis, R.; Muthumary, J.; Silver, B.; Bright, P.; Dichlorotriazine, R. Antibacterial activity of silver nanoparticles synthesized from serine. *Mater. Sci. Eng. C* **2014**, *49*, 316–322. [[CrossRef](#)]
55. Sanpui, P.; Murugadoss, A.; Prasad, P.V.D.; Ghosh, S.S.; Chattopadhyay, A. The antibacterial properties of a novel chitosan-Ag-nanoparticle composite. *Int. J. Food Microbiol.* **2008**, *124*, 142–146. [[CrossRef](#)]
56. National Center for Environmental Assessment. *Integrated Risk Information System (IRIS) Chemical Assessment Summary: Silver*; CASRN 7440-22-4; National Center for Environmental Assessment: Oakbrook Terrace, IL, USA, 2003.
57. Rtimi, S.; Kiwi, J.; Karimi, A.; Sanjinés, R. Innovative Ti1–xNbxN–Ag Films Inducing Bacterial Disinfection by Visible Light/Thermal Treatment. *ACS Appl. Mater. Interfaces* **2018**, *10*, 12021–12030. [[CrossRef](#)] [[PubMed](#)]
58. Hajjaji, A.; Elabidi, M.; Trabelsi, K.; Assadi, A.A.; Bessais, B.; Rtimi, S. Bacterial adhesion and inactivation on Ag decorated TiO<sub>2</sub>-nanotubes under visible light: Effect of the nanotubes geometry on the photocatalytic activity. *Colloids Surf. B Biointerfaces* **2018**, *170*, 92–98. [[CrossRef](#)] [[PubMed](#)]

59. Rtimi, S.; Nadochenko, V.; Khmel, I.; Bensimon, M.; Kiwi, J. First unambiguous evidence for distinct ionic and surface-contact effects during photocatalytic bacterial inactivation on Cu–Ag films: Kinetics, mechanism and energetics. *Mater. Today Chem.* **2017**, *6*, 62–74. [[CrossRef](#)]
60. Chernozem, R.V.; Surmeneva, M.A.; Krause, B.; Baumbach, T.; Ignatov, V.P.; Tyurin, A.I.; Loza, K.; Epple, M.; Surmenev, R.A. Hybrid biocomposites based on titania nanotubes and a hydroxyapatite coating deposited by RF-magnetron sputtering: Surface topography, structure, and mechanical properties. *Appl. Surf. Sci.* **2017**, *426*, 229–237. [[CrossRef](#)]
61. Niinomi, M.; Nakai, M.; Hieda, J. Development of new metallic alloys for biomedical applications. *Acta Biomater.* **2012**, *8*, 3888–3903. [[CrossRef](#)]
62. Crawford, G.A.; Chawla, N.; Das, K.; Bose, S.; Bandyopadhyay, A. Microstructure and deformation behavior of biocompatible TiO<sub>2</sub> nanotubes on titanium substrate. *Acta Biomater.* **2007**, *3*, 359–367. [[CrossRef](#)]
63. Manoj Kumar, R.; Kuntal, K.K.; Singh, S.; Gupta, P.; Bhushan, B.; Gopinath, P.; Lahiri, D. Electrophoretic deposition of hydroxyapatite coating on Mg-3Zn alloy for orthopaedic application. *Surf. Coat. Technol.* **2016**, *287*, 82–92. [[CrossRef](#)]
64. Hang, Y.; Liu, G.; Huang, K.; Jin, W. Mechanical properties and interfacial adhesion of composite membranes probed by in-situ nano-indentation/scratch technique. *J. Membr. Sci.* **2015**, *494*, 205–215. [[CrossRef](#)]
65. Mali, S.; Misra, R.D.K.; Somani, M.C.; Karjalainen, L.P. Biomimetic nanostructured coatings on nano-grained/ultrafine-grained substrate: Microstructure, surface adhesion strength, and biosolubility. *Mater. Sci. Eng. C* **2009**, *29*, 2417–2427. [[CrossRef](#)]
66. Bartmanski, M.; Cieslik, B.; Glodowska, J.; Kalka, P. Electrophoretic deposition (EPD) of nanohydroxyapatite—Nanosilver coatings on Ti<sub>13</sub>Zr<sub>13</sub>Nb alloy. *Ceram. Int.* **2017**, *43*, 11820–11829. [[CrossRef](#)]
67. Tozar, A.; Karahan, İ.H. A comparative study on the effect of collagen and h-BN reinforcement of hydroxyapatite/chitosan biocomposite coatings electrophoretically deposited on Ti-6Al-4V biomedical implants. *Surf. Coat. Technol.* **2018**, *340*, 167–176. [[CrossRef](#)]
68. Tozar, A.; Karahan, İ.H. A comprehensive study on electrophoretic deposition of a novel type of collagen and hexagonal boron nitride reinforced hydroxyapatite/chitosan biocomposite coating. *Appl. Surf. Sci.* **2018**, *452*, 322–336. [[CrossRef](#)]
69. Cordero-Arias, L.; Cabanas-Polo, S.; Gao, H.; Gilibert, J.; Sanchez, E.; Roether, J.A.; Schubert, D.W.; Virtanen, S.; Boccaccini, A.R. Electrophoretic deposition of nanostructured-TiO<sub>2</sub>/chitosan composite coatings on stainless steel. *RSC Adv.* **2013**, *3*, 11247–11254. [[CrossRef](#)]
70. Kasraei, S.; Azarsina, M. Addition of silver nanoparticles reduces the wettability of methacrylate and silorane-based composites. *Braz. Oral Res.* **2012**, *26*, 505–510. [[CrossRef](#)]

